J. Fluid Mech. (1998), *vol.* 360, *pp.* 249–271. Printed in the United Kingdom

Low-Reynolds-number flow around an oscillating circular cylinder at low Keulegan–Carpenter numbers

By H. DÜTSCH, F. DURST, S. BECKER AND H. LIENHART

Institute of Fluid Mechanics, University of Erlangen–Nuremberg, Cauerstrasse 4, D–91058 Erlangen, Germany

(Received 18 February 1997 and in revised form 26 November 1997)

Time-averaged LDA measurements and time-resolved numerical flow predictions were performed to investigate the laminar flow induced by the harmonic in-line oscillation of a circular cylinder in water at rest. The key parameters, Reynolds number Re and Keulegan–Carpenter number KC, were varied to study three parameter combinations in detail. Good agreement was observed for $Re = 100$ and $KC = 5$ between measurements and predictions comparing phase-averaged velocity vectors. For $Re = 200$ and $KC = 10$ weakly stable and non-periodic flow patterns occurred, which made repeatable time-averaged measurements impossible. Nevertheless, the experimentally visualized vortex dynamics was reproduced by the two-dimensional computations. For the third combination, $Re = 210$ and $KC = 6$, which refers to a totally different flow regime, the computations again resulted in the correct fluid behaviour. Applying the widely used model of Morison *et al.* (1950) to the computed in-line force history, the drag and the added-mass coefficients were calculated and compared for different grid levels and time steps. Using these to reproduce the force functions revealed deviations from those originally computed as already noted in previous studies. They were found to be much higher than the deviations for the coarsest computational grid or the largest time step. The comparison of several in-line force coefficients with results obtained experimentally by Kühtz (1996) for $\beta = 35$ confirmed that force predictions could also be reliably obtained by the computations.

1. Introduction

The research field of fluid–structure interaction is attracting increased attention from fluid mechanics researchers as well as structural engineers. The development of new measuring techniques that provide detailed information about the time variations of local flow properties are stirring this new interest in a field which has seen active research efforts for many decades. Furthermore, new developments in numerical methods and increased hardware performance have resulted in advanced computer facilities which allow the experimental investigations to be supported by fluid flow computations. Their aim is to provide information on the time-dependent loading of structures due to their interaction with surrounding fluids. Research results are mainly needed for the design of structures and reliability controls. The methods currently employed are based on analytical or semi-empirical models requiring force coefficients from the experimental and numerical work on individual fluid flow–structure interactions.

Circular cylinders in cross-flow or the motion of circular cylinders in a fluid at rest are especially of interest in fields such as offshore and civil engineering or heat exchanger design in particular. Such flows were investigated by e.g. Keulegan & Carpenter (1958), Sarpkaya (1976), Williamson (1985), Obasaju, Bearman & Graham (1988) as well as by Tatsuno & Bearman (1990) and Justesen (1991). The recent investigations by Sarpkaya (1992), Anagnostopoulos, Iliadis & Ganoulis (1995) and Lin, Bearman & Graham (1996) should be mentioned among others. A good overview of engineering applications is given in the book by Naudascher & Rockwell (1994). Such flows are mainly ruled by complex vortex–vortex and vortex–structure interaction phenomena involving stability problems, bifurcations and three-dimensional patterns. Hence, time-dependent computations have to be carried out carefully at low Reynolds numbers. However there is a lack of experimental data to confirm and verify numerical results.

It is general practice to provide the required information for the design of fluid-exposed structures through experimental studies, measuring the forces on the structure for a prescribed motion either of the fluid or of the structure. One comprehensive model to describe the in-line motion of an elastically mounted structure, exposed to excitations by a fluid flow, is the following equation:

$$m_0 \ddot{x}_1 + 2 m_0 \zeta_0 \omega_0 \dot{x}_1 + k_{x_1} x_1 = \rho S c_m \dot{U}_1 - \rho S c_i \ddot{x}_1 + \tfrac{1}{2} \rho D c_d (U_1 - \dot{x}_1) |U_1 - \dot{x}_1| , \quad (1.1)$$

see Blevins (1977). Here m_0 is the structure mass per unit length, x_1 the displacement, ζ_0 the damping coefficient of the structure, ω_0 the circular natural frequency of the structure without fluid surrounding it and k_{x_1} the stiffness parameter. The fluid density is denoted by ρ, the cross-sectional area by S, the excitation velocity by U_1, and D is a characteristic length, e.g. the diameter. According to the widely used approach of Morison *et al.* (1950), three force parameters are included in this equation, the drag coefficient c_d, the inertia coefficient c_m and the added-mass coefficient c_i, with

$$c_m = c_i + 1.0 . \quad (1.2)$$

Here the increase of 1.0 is the result of the uniform pressure gradient occurring in a globally accelerated flow. Applying equation (1.1) to the oscillatory motion of a circular cylinder in a quiescent fluid, the time-dependent in-line force F_1 per unit length acting on the cylinder can be expressed as

$$F_1(t) = -\tfrac{1}{2} \rho D c_d \dot{x}_1 |\dot{x}_1| - \tfrac{1}{4} \pi \rho D^2 c_i \ddot{x}_1 , \quad (1.3)$$

where t denotes the time. Exciting a cylinder with a prescribed motion $x_1(t)$ and measuring $F_1(t)$ allows the motion-averaged c_i and c_d coefficients to be evaluated by methods such as least-squares fitting or by Fourier analysis. Constant values of c_i and c_d are derived from such experiments, and by similarity analysis generalization of the results is achieved, showing that both coefficients depend on the Reynolds number Re and the Keulegan–Carpenter number KC. These key numbers are defined as

$$Re = \frac{U_{max} D}{\nu} \quad \text{and} \quad KC = \frac{U_{max}}{f D} , \quad (1.4)$$

where U_{max} is the maximum velocity of the cylinder motion, ν the kinematic fluid viscosity and f a characteristic frequency. The ratio $\beta = Re/KC$, which is denoted the Stokes parameter or viscous scale parameter, is an alternative key parameter and was first introduced by Sarpkaya (1976). In the present study the translational motion

$x_1(t)$ is given by the harmonic oscillation

$$x_1(t) = -A \sin(2\pi f t) , \tag{1.5}$$

where A denotes the amplitude of the cylinder motion. Thus the Keulegan–Carpenter number can be written as

$$KC = \frac{2\pi A}{D} . \tag{1.6}$$

There have been numerous investigations using the right-hand side of equation (1.1) to obtain c_i, c_m and c_d through experimental techniques, e.g. see Sarpkaya (1976, 1986), Troesch & Kim (1991), Bearman, Lin & Mackwood (1992) and in recent times Kühtz, Bearman & Graham (1997). Some of these experiments have been accompanied by analytical investigations and lately by numerical studies, see Bearman *et al.* (1985), Stansby & Smith (1991), Sarpkaya *et al.* (1992), Sarpkaya (1992) as well as the work of Newman & Karniadakis (1995) and Lin *et al.* (1996). The latter have benefited from recent advances in numerical techniques and by the increased computer power. Combining advanced numerical methods, e.g. multigrid solvers, and increased computer power, e.g. by parallel computing, allows direct numerical studies of the fluid motion induced by an oscillating cylinder. Additionally, the resulting forces, needed to drive the cylinder or acting on it, can easily be obtained from the computations. This outlook, to have increasingly advanced computer codes available in the future, motivated the investigations described in this paper. It was the aim of this work to provide detailed experimental velocity information and, hence, to prove that numerical flow predictions can be used to predict reliably the fluid motion and the forces induced by an oscillating cylinder. The numerical method applied is described in § 2.

To carry out verification experiments, the authors employed laser Doppler anemometry (LDA) to yield time traces of the local velocities. From these measurements, phase-averaged velocity information was deduced (see § 3) and compared with the corresponding numerical data. Results are presented in § 4 and conclusions in § 5 including an outlook on future research.

The authors are pleased to provide the experimental data sets for $Re = 100$ and $KC = 5$ on request. Computer animations (Raster Metafile) for the three mainly investigated cases are available directly from the authors (duetsch@lstm.uni-erlangen.de) as well as mpeg files on the Internet site http://www.lstm.uni-erlangen.de/ma3/hduetsch_e.html.

2. Numerical computations

It was the aim of the computational study to predict the two-dimensional fluid motion induced by the oscillation of a circular cylinder. Considering the cylinder motion in water at rest, two reference frames suggested themselves for the problem description. One, the inertial system x_i, is connected to the stationary fluid tank. The other moves with the cylinder and is therefore an accelerated reference system with its Cartesian coordinates denoted $\tilde{x}_i$. While the first approach was used in the experiments, the second provided advantages for the computations. Both were connected by the well known relationship

$$x_i = \tilde{x}_i + x_{i,s} . \tag{2.1}$$

Here $x_{i,s}$ denotes the position of the accelerated reference system and is given by

$$x_{1,s}(t) = x_1(t)\,, \tag{2.2}$$

$$x_{2,s}(t) = 0\,. \tag{2.3}$$

Differentiating equation (2.1) in time, the velocity U_i of a fluid element in the inertial system can be written as

$$U_i(t) = \tilde{U}_i(t) + U_{i,s}(t)\,. \tag{2.4}$$

Here $\tilde{U}_i$ denotes the fluid velocity in the accelerated reference system and $U_{i,s}(t)$ the corresponding system velocity, i.e. the cylinder velocity. Hence, the fundamental fluid mechanics equations for constant density ρ, which was 998.2 kg m^3 in all computations, for the accelerated system and for a two-dimensional flow field are

$$\frac{\partial \tilde{U}_1}{\partial \tilde{x}_1} + \frac{\partial \tilde{U}_2}{\partial \tilde{x}_2} = 0\,, \tag{2.5}$$

$$\rho\left[\frac{\partial \tilde{U}_1}{\partial t} + \tilde{U}_1\frac{\partial \tilde{U}_1}{\partial \tilde{x}_1} + \tilde{U}_2\frac{\partial \tilde{U}_1}{\partial \tilde{x}_2}\right] = -\frac{\partial P}{\partial \tilde{x}_1} + \mu\left[\frac{\partial^2 \tilde{U}_1}{\partial \tilde{x}_1^2} + \frac{\partial^2 \tilde{U}_1}{\partial \tilde{x}_2^2}\right] - \rho\frac{\mathrm{d}U_{1,s}}{\mathrm{d}t} \tag{2.6}$$

and

$$\rho\left[\frac{\partial \tilde{U}_2}{\partial t} + \tilde{U}_1\frac{\partial \tilde{U}_2}{\partial \tilde{x}_1} + \tilde{U}_2\frac{\partial \tilde{U}_2}{\partial \tilde{x}_2}\right] = -\frac{\partial P}{\partial \tilde{x}_2} + \mu\left[\frac{\partial^2 \tilde{U}_2}{\partial \tilde{x}_1^2} + \frac{\partial^2 \tilde{U}_2}{\partial \tilde{x}_2^2}\right]. \tag{2.7}$$

Here, P is the pressure and μ the dynamic viscosity, which was 1.008 18 mPas for all computations. Considering the momentum equations (2.6) and (2.7) in the non-inertial reference frame, the term $-\rho\,\mathrm{d}U_{1,s}/\mathrm{d}t$ had to be added, taking the system acceleration into account.

For the numerical predictions the second approach was chosen in order to perform computations more efficiently. Applying the general equations in the inertial system, the numerical grid had to be moved and adjusted from time step to time step according to the cylinder motion. But from the cylinder's point of view the grid did not need to be changed during the computations because of the chosen cylinder-fixed coordinate system. Additional computational time had to be spent finally to retransform the velocity vector field into the inertial system by adding the system velocity $U_{i,s}$ as well as for calculation of the actual location of the grid points by adding the position vector $x_{i,s}(t)$ of the system; see equations (2.1) and (2.4). As both transformations could be done algebraically, little computational effort had to be spent on these operations, which was the main advantage of the computational approach. It was a valid approach for the present study, as the cylinder walls were dimensionally stable and the influence of the outer walls of the water tank was negligible. Furthermore, for future studies, this numerical treatment of moving boundaries can easily be extended to different shapes of structures or arrays of structures, to combinations of oscillating flow and oscillating structures as well as to arbitrary kinematic functions of motion.

The boundary conditions were changed from the original viewpoint of a flow induced by the motion of a cylinder to oscillating flow around a cylinder at rest. The fluid velocity at the outer boundary $\tilde{U}_{i,b}$ oscillated with the negative cylinder velocity, and on the cylinder surface the no-slip condition was assumed as if investigating oscillating flow around a cylinder at rest:

$$\tilde{U}_{i,b} = U_{i,b} - U_{i,s}(t)\,. \tag{2.8}$$

For the numerical investigations an adapted version of the computer code FASTEST-

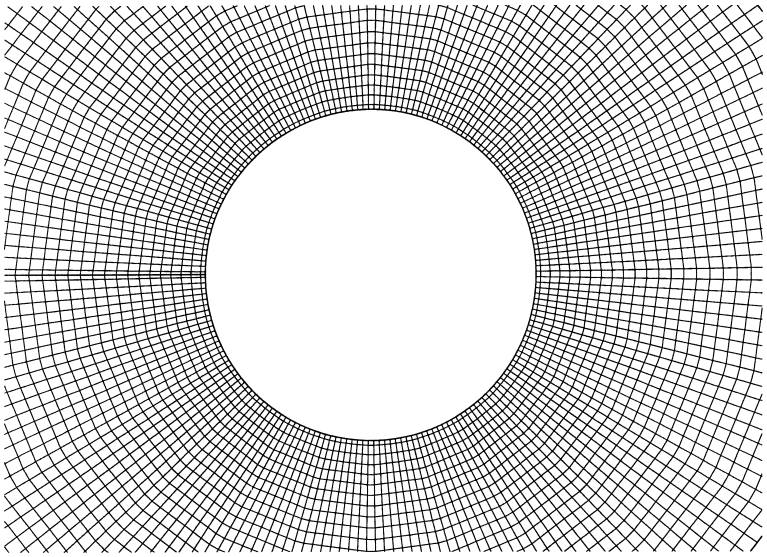

FIGURE 1. Centre region of one computational grid consisting of concentric circles (192 control volumes along cylinder perimeter). Outer diameter 120 times cylinder diameter.

2D was applied; see FASTEST-2D. It employed a finite volume discretization and a SIMPLE-like algorithm for the pressure–velocity correction proposed by Patankar (1980). Furthermore, a multigrid technique was included to speed up convergence with a performance that was described in detail by Durst *et al.* (1993). The convection term was approximated by a central difference scheme of second order. In order to yield the same order of accuracy in time, the time derivatives in equation (2.6) and in equation (2.7) were consistently discretized by the Crank–Nicolson formulation. Therefore, the numerical method applied was of second order in space and time. The set of equations was then solved on an O-type structured grid with a non-staggered arrangement of the variables; see figure 1 and details in § 4.1. For each time step and each variable the residual had to decrease at least five orders of magnitude, which was in agreement with the findings of Lin *et al.* (1996). Hence, in computing one time step on a grid with 24 576 control volumes about 385 s CPU time had to be spent on a workstation of about 13 MFlops sustained performance rate. Applying the multigrid technique with three coarser grid levels the total computing time was reduced to 95 s.

The present flow configuration had two characteristic time scales:
time scale of diffusive transport

$$t_{diff} = \frac{D^2}{\nu}, \tag{2.9}$$

time scale of convective transport

$$t_{conv} = \frac{D}{U_{max}}. \tag{2.10}$$

Considering the Reynolds number as the ratio of both time scales, the convective time scale t_{conv} for $Re = t_{diff}/t_{conv} = 100$ was approximately 1 s. With 720 time steps per cycle of oscillation, the length of the time steps Δt was about 0.0069 s and, hence, sufficiently small to yield time-accurate predictions of the fluid motion. Additionally,

computations with a 4 times and a 12 times greater time step were performed as well as computations on different grid levels. The comparison of the results is presented in § 4.1.

Regarding the kinematic equation (1.5), the calculations started in fact one quarter of a cycle earlier so that the cylinder position was at its maximum amplitude and the cylinder started from rest. No artificial disturbances were employed to introduce flow instability effects on the computations.

The computations carried out in this work provided time-dependent, discrete pressure and velocity distributions. For the validation of the computational results, both velocity components were compared in detail with the experimental results (see § 4.1).

Furthermore, from the velocity field the vorticity

$$\Omega = \frac{\partial u_i}{\partial x_j} - \frac{\partial u_j}{\partial x_i}, \quad \text{with } i = 1 \text{ and } j = 2, \tag{2.11}$$

was calculated as an area-weighted mean value $\bar{\Omega}$. Considering

$$\bar{\Omega} = \frac{1}{S} \int \Omega \mathrm{d}S \, , \tag{2.12}$$

where S denotes an area, and applying Stokes theorem, $\bar{\Omega}$ resulted in the form

$$\bar{\Omega} = \frac{1}{S} \left(\oint u_1 \mathrm{d}x_1 + \oint u_2 \mathrm{d}x_2 \right) \, . \tag{2.13}$$

Equation (2.13) was evaluated along each control volume boundary assuming constant velocities at each surface. From the computed vorticity distribution vortex shedding and vortex motion could easily be recognized. It was therefore evaluated to determine the time-dependent vortex dynamics induced by the oscillating cylinder. Fundamentally different mechanisms were revealed for the three flow regimes investigated in detail, e.g. see Williamson (1985) and Tatsuno & Bearman (1990).

The pressure distribution was determined directly by the computational method. Hence, by integrating the surface pressure and shear stress acting on the cylinder the in-line and the lift forces per unit length were computed. By applying a Fourier analysis to the in-line force history according to equation (1.3), the force coefficients c_d and c_i were calculated. They were compared with the experimental results of Kühtz (1996) for $\beta = 35$.

3. Experimental techniques

The test rig built for the present studies consisted in principle of a stationary tank with fluid at rest, in which the cylinder was sinusoidally actuated by a crank shaft gear drive. Figure 2 shows its major components: the water tank, the cylinder, the drive system, and the LDA probe mounted on the top of the two-dimensional traversing units. The overall dimensions of the water tank were $1.2 \times 0.7 \times 0.7$ m^3, and the diameter of the cylinder used for the investigations was 10 mm and its length 0.65 m. Any influence of the flow field boundaries has been neglected for all the results described later. In order to achieve the different non-dimensional characteristic numbers Re and KC, there were three experimental parameters that could be adjusted: the rotational speed of the motor drive, the amplitude of oscillation of the gear drive and the diameter of the cylinder. The rotational speed was controlled by the supply voltage for the DC motor, the amplitude of oscillation resulted from

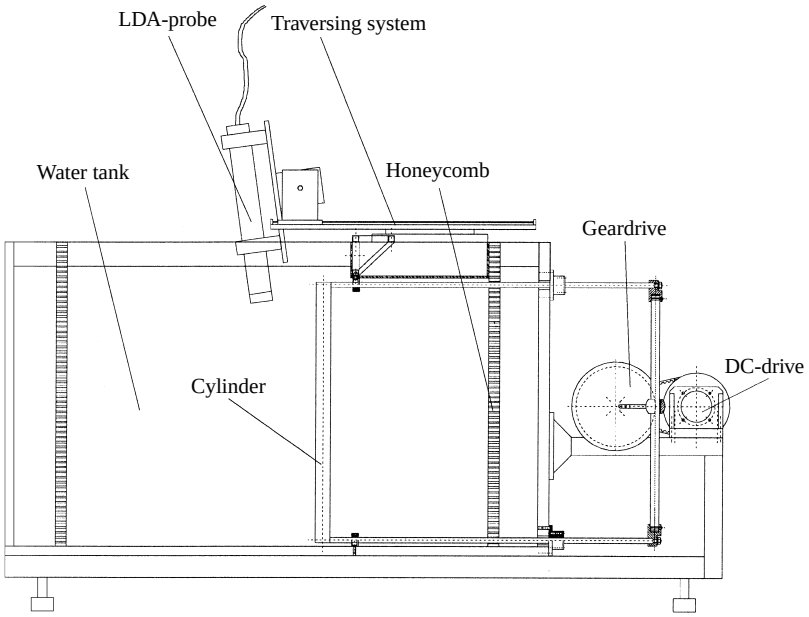

FIGURE 2. Test rig in cross-section.

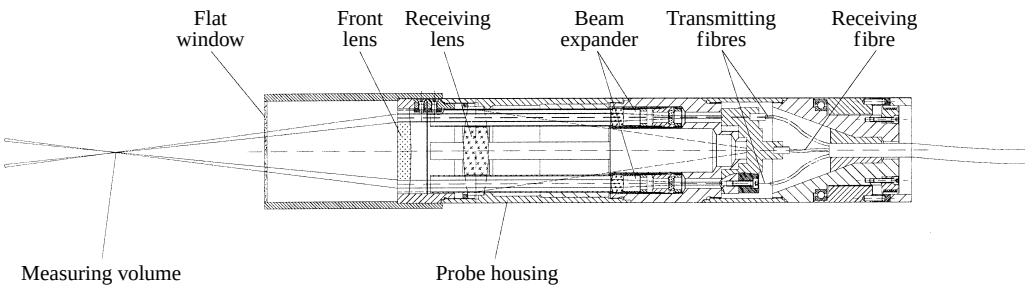

FIGURE 3. Cross-sectional view of glass-fibre LDA probe.

the off-centre position of the eccenter drive. During the setting up of the experiment and the initial tests, emphasis was placed on a smooth and uniform sinusoidal motion of the cylinder, avoiding any distortion by vibration or stick-slip effects.

The LDA adopted was a slightly modified LDA system built at LSTM for wind tunnel applications; see Lienhart & Böhnert (1992). It consisted of a glass fibre LDA probe head and a LDA base unit. The base unit incorporated the Ar ion laser light source, the beam and colour separators, the Bragg cells and the fibre couplers, thus providing two blue (488 nm) and two green (515 nm) frequency-shifted laser beams. The laser beams were transmitted by monomode polarization preserving glass fibres to the LDA probe, which is shown in cross-sectional view in figure 3. It created a measuring control volume of about 40 μm diameter at a working distance of 235 mm from the front lens in water. This allowed simultaneous two-component velocity measurements in backscatter mode.

The electronics applied for LDA signal acquisition were two BSAs (Burst Spectrum Analyzers) from DANTEC. The crank shaft angle was detected by two light barrier pulse encoders mounted on the crank shaft. They delivered TTL pulses for 1° and

360°, respectively, referring to the gear drive system. Their signals were interpreted by a phase-locked loop electronic system, which was connected to the BSA units. The angle information was transmitted together with the aquired velocity components to the computer that also controlled the traversing system, thus allowing for angle/phase-resolved velocity measurements in the flow field around the oscillating cylinder.

For a well-defined grid of measuring points fixed to the stationary fluid tank, the LDA system was mounted on the test rig at the top of a two-dimensional traversing unit. The measuring grid used was equidistant in the x_1- and x_2-directions with a mesh size of 2 mm × 1 mm. In order to obtain valid data in the vicinity of the cylinder surface, the probe was slightly tilted, and the velocity information was transformed into the coordinate system perpendicular to the cylinder axis. The acquired raw data, which were measured at one spatial point over the phase angle, were processed, statistically reduced by averaging the LDA measurements within increments of 1° of crank shaft angle, and rearranged in such a way that fields of flow velocity vectors for all phase angles resulted. As it was not possible to acquire enough data for accurate statistics within one cycle of oscillation, averages over several cycles were employed. For the final data set it was decided to take 72 000 validated velocity measurements per grid node, i.e. 200 samples per grid node and per degree of phase angle. As the flow was laminar and therefore the variance of the data low, this turned out to be sufficient. However, with a period of the oscillation of about 5 s for the first parameter combination $Re = 100$ and $KC = 5$, this resulted in an overall measuring time of about 3 min per grid point and about 40 h for a complete survey of the flow field. An artificial flow visualization computer animation was created from the results of the velocity measurements, that showed the local vorticity distribution in background colours. The vorticity field was derived by relationships (2.11) to (2.13) as applied for the numerical results. This animation gave an excellent overview and insight into the complex time-dependent flow field and allowed an assessment of the measured data.

Not shown in figure 2 is the instrumentation used for visualization of the flow patterns induced by the oscillating cylinder. The technique adopted was the injection of dye on the circumference of the cylindrical rod. Three taps of diameter 0.3 mm were placed in the horizontal symmetry plane at 0°, 90°, and 270° relative to the direction of oscillation and they were fed with drawing ink from inside the rod. The streak lines in the flow field were observed and registered by video from above.

4. Results and discussion

4.1. *Results for* $Re = 100$ *and* $KC = 5$

The flow around an oscillating cylinder can be complex, showing vortex structures and mechanisms with different properties and different behaviours. These findings led Tatsuno & Bearman (1990) to propose the flow regime diagram sketched in figure 4. The suggested flow regimes in this figure were reproduced in sample experiments by Knörnschild (1994) carried out at the authors' institute. These experiments prepared the basis for the investigations described in this paper.

The first parameter set of the present investigation was $Re = 100$ and $KC = 5$, corresponding to regime A as proposed by Tatsuno & Bearman (1990), see figure 4. Flow resulting for this parameter combination was characterized by stable, symmetric and periodic vortex shedding as shown in figure 5. Detailed studies by means of flow visualization showed that the resulting flow was two-dimensional, providing stable vortex shedding and two fixed stagnation points at the front and back of the cylinder.

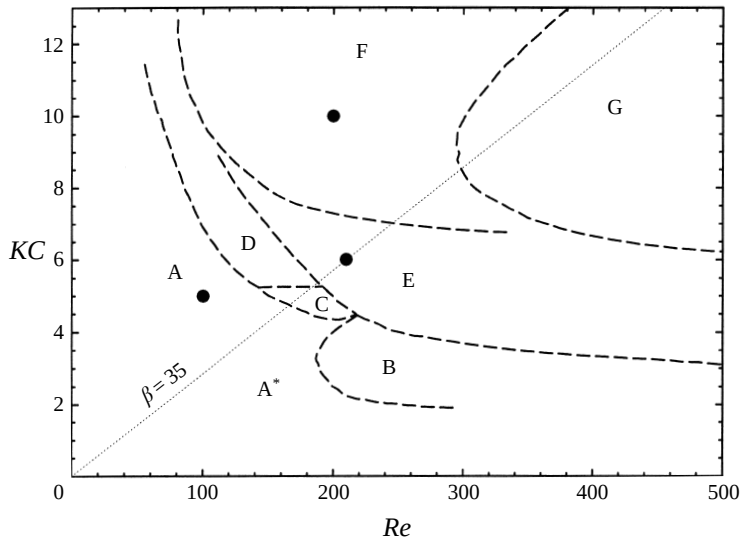

FIGURE 4. Flow regimes defined by Tatsuno & Bearman (1990).

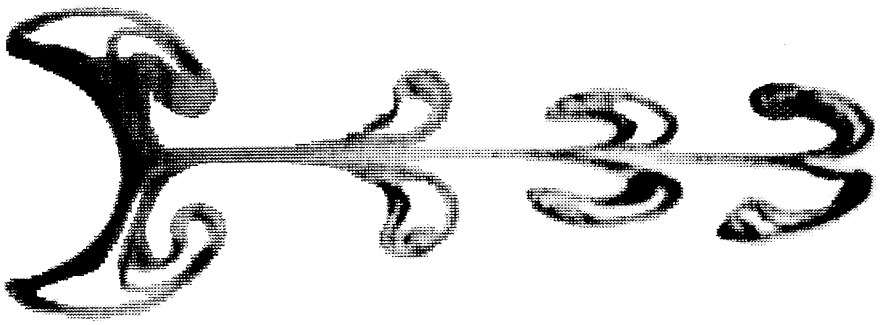

FIGURE 5. Flow visualization for $Re = 100$ and $KC = 5$.

The resulting vortex dynamics could be described as follows. As the oscillating cylinder moved in the forward direction, at the front of the cylinder an upper and lower boundary layer flow developed, which separated at the same upper and lower position on the cylinder wall. The separating flow produced two counter-rotating vortices of apparently the same magnitude of strength, and hence resulting in the same vortex shape. This vortex production was coming to an end when the maximum front location of the cylinder was reached and the cylinder started its backward motion, creating the same vortex formation on the other side of the cylinder, i.e. in the new wake of the cylinder flow. In addition, the backward motion of the cylinder caused a splitting of the vortex pair, which was produced by the forward motion, and finally wake reversal occurs. A sequence of this periodic flow pattern caused by the forward and backward motion is shown in figure 5.

Carrying out time-dependent two-dimensional flow calculations allowed the fluid motion in figure 5 to be numerically reproduced. This is reflected by the set of data presented in figure 6, showing pressure and vorticity isolines for different phase angles of the oscillating cylinder motion.

The numerical predictions of vorticity isolines, in particular, reflect the vortex

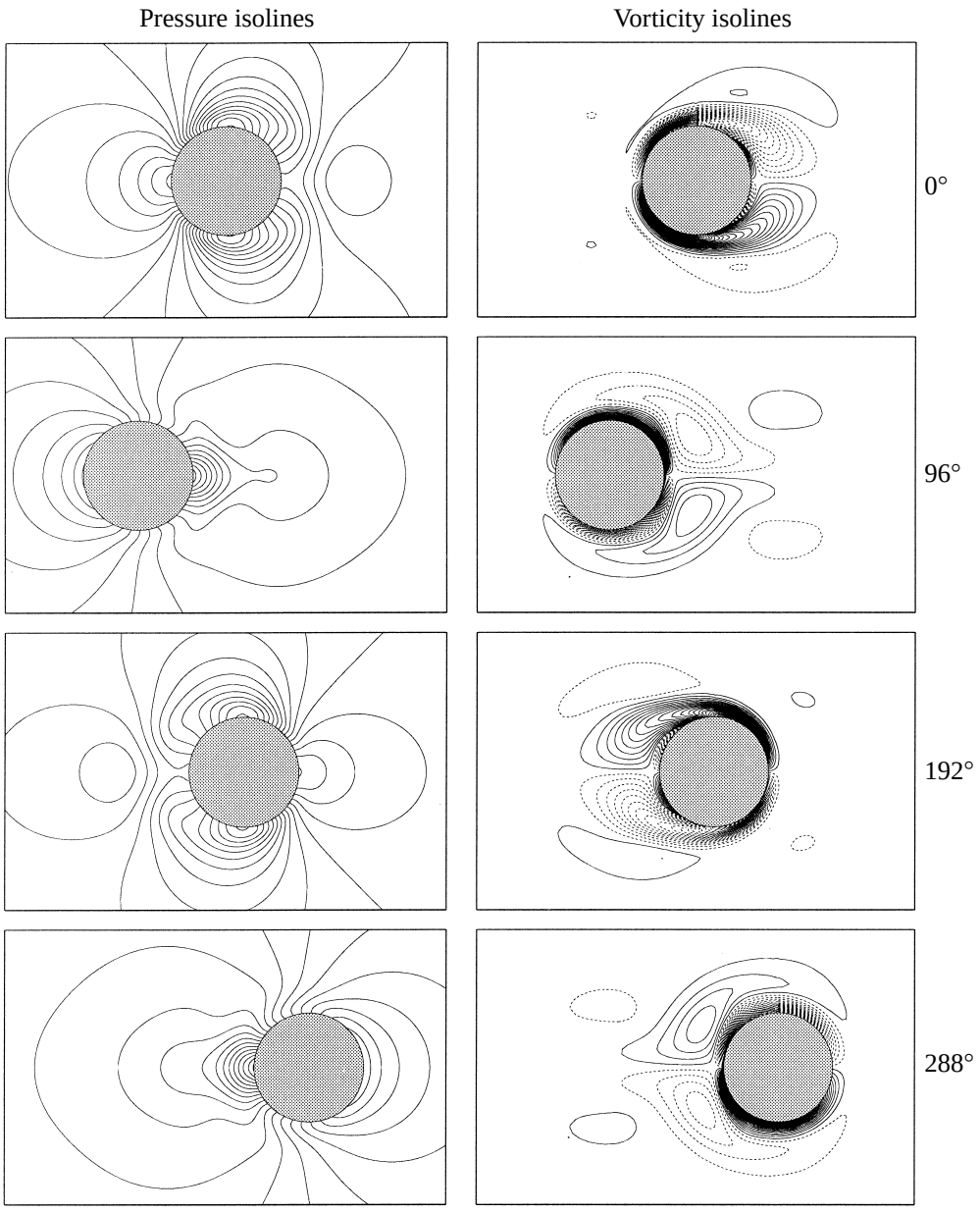

FIGURE 6. Pressure and vorticity isolines (negative values dashed) at $Re = 100$ and $KC = 5$.

formation during the forward and backward motion of the oscillating cylinder. The good agreement between the experimental and numerical results is also indicated by the comparisons provided in figure 7 of measured and predicted velocity fields for three angles of the cylinder motion. To compare further the experimental and numerical results, the data were processed to yield local phase-averaged velocity information. Data are provided in figure 8 for three phase angles of the oscillatory cylinder motion, showing velocity profiles at four locations for constant x_1-position. The comparison is considered to be very satisfactory and therefore the authors are able to recommend

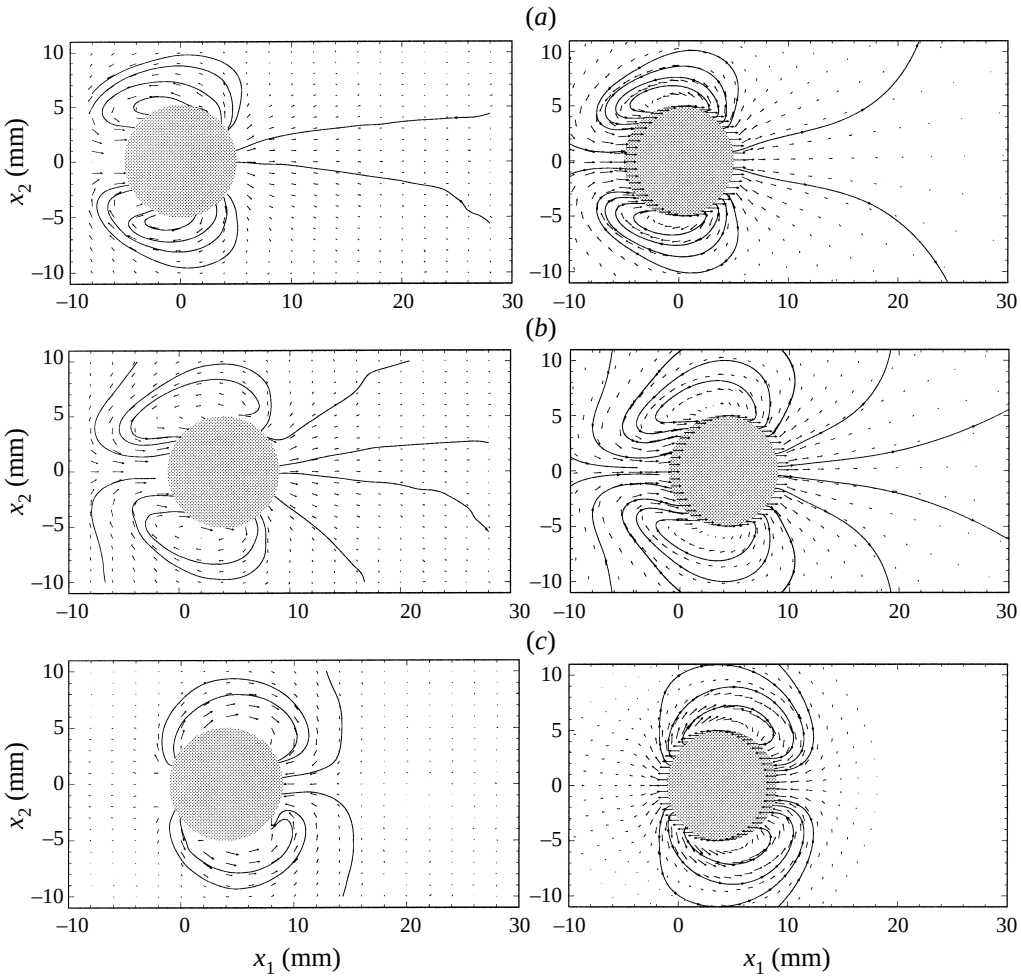

FIGURE 7. Measured (left) and computed (right) velocity vectors and streamlines in the vicinity of the cylinder at $Re = 100$ and $KC = 5$ for (*a*) 180°, (*b*) 210° and (*c*) 330°.

the application of numerical prediction procedures to yield detailed information on the fluid motion induced by oscillating cylinders, at least for low Re and KC.

The numerical predictions were analysed with respect to the independence of the spatial grid size and the computational time step. It was found that the numerical data were sufficiently accurate to yield very reliable force information. Hence the in-line force $F_1(t)$ of the oscillatory motion of the cylinder could be computed and the resulting information be employed to calculate the c_d and the c_i coefficients of equation (1.3). Utilizing these coefficients allows the in-line force $F_1(t)$ to be approximately computed through equation (1.3), as is currently done in practice. As is shown below, $F_1(t)$ could be obtained directly from the numerical flow predictions, yielding precise information on the time variation and on the contributory parts, i.e. the pressure and shear part, of the in-line force.

By evaluating the numerical results for various grid sizes and computational time steps Δt, the in-line force was computed yielding the results presented in table 1 for $Re = 100$ and $KC = 5$. This table contains information for various grid sizes and

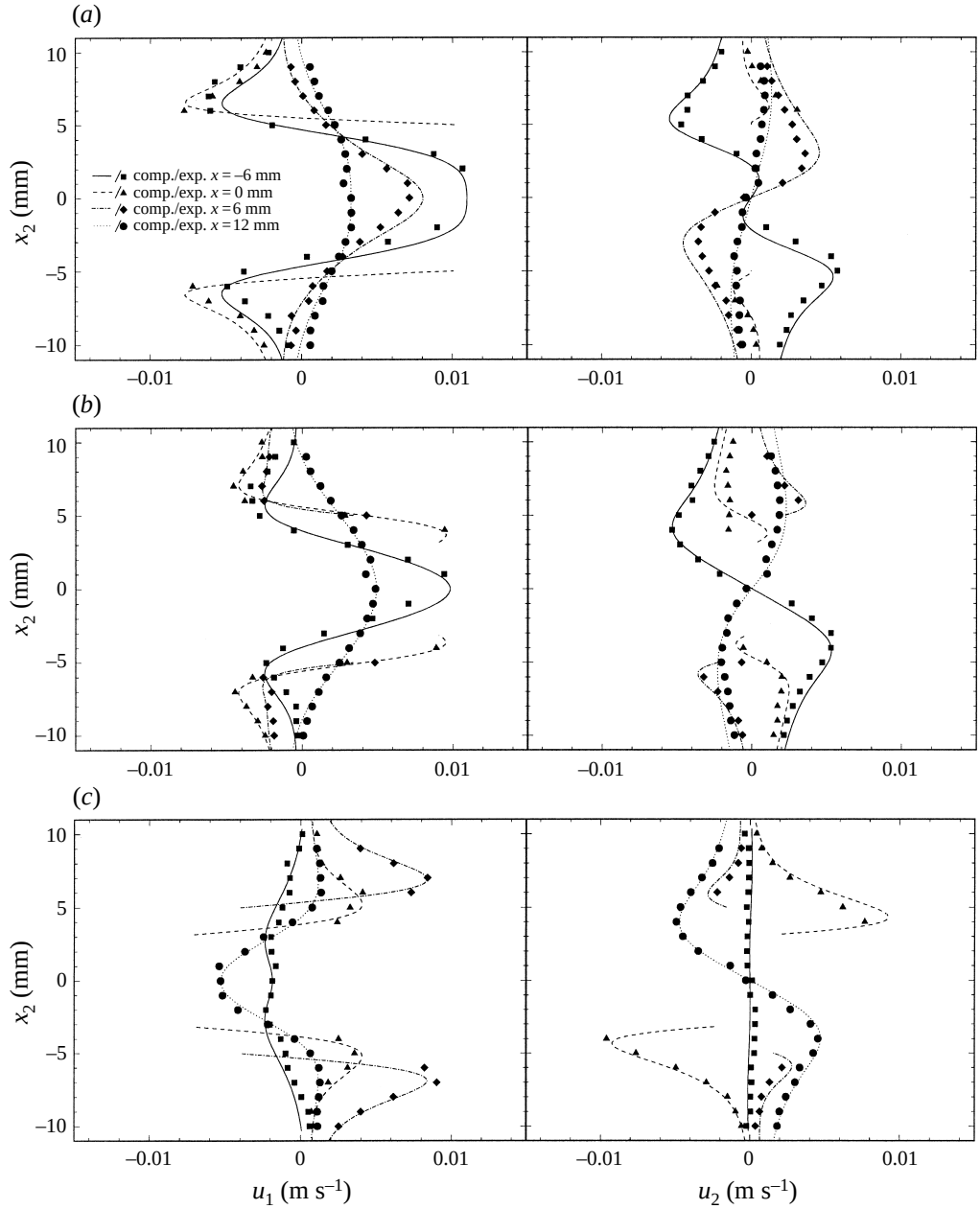

FIGURE 8. Comparison of the velocity components at four cross-sections with constant x_1-value. Phase position (*a*) 180°, (*b*) 210° and (*c*) 330°.

time steps, where $\#\mathrm{cv}_{perimeter}$ is the number control volumes on the cylinder perimeter and $\#\mathrm{cv}_{total}$ is the total number of control volumes employed. Here $\Delta t/T$ denotes the normalized time step per period of oscillation and, hence, provides information on the time resolution of the numerical predictions. For the best spatial resolutions and the smallest time steps of the predictions, case C, the c_d and c_i values are $c_d = 2.09$ and $c_i = 1.45$.

	$Re = 100,\ KC = 5$					$Re = 200,\ KC = 10$	
Set	A	B1	C	B2	B3	D1	D2
c_d	2.15	2.10	2.09	2.15	2.17	1.81–1.84	1.82–1.89
c_i	1.42	1.45	1.45	1.42	1.41	1.02–1.04	0.92–0.97
$\#\text{cv}_{perimeter}$	96	192	384	192	192	192	192
$\#\text{cv}_{total}$	6144	24 576	98 304	24 576	24 576	24 576	24 576
$\Delta t/T$	1/720	1/720	1/720	1/180	1/60	1/720	1/60

TABLE 1. Drag and added-mass coefficients fitted to different computational results.

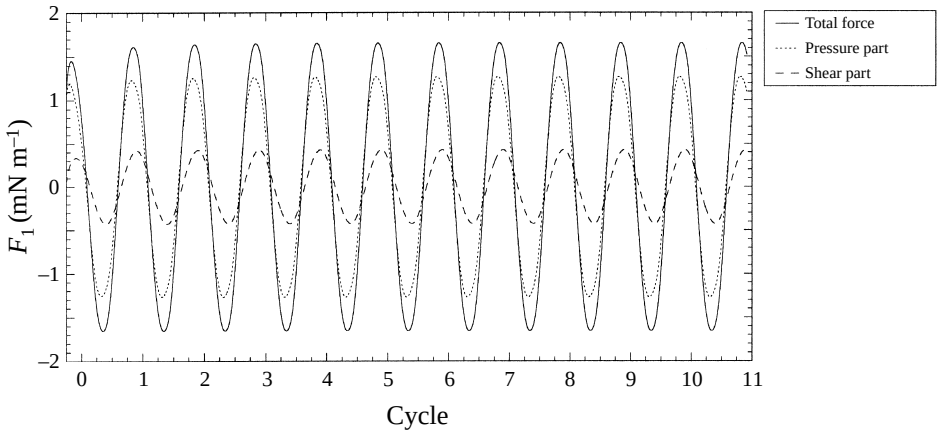

FIGURE 9. In-line force history at $Re = 100$ and $KC = 5$ (set C).

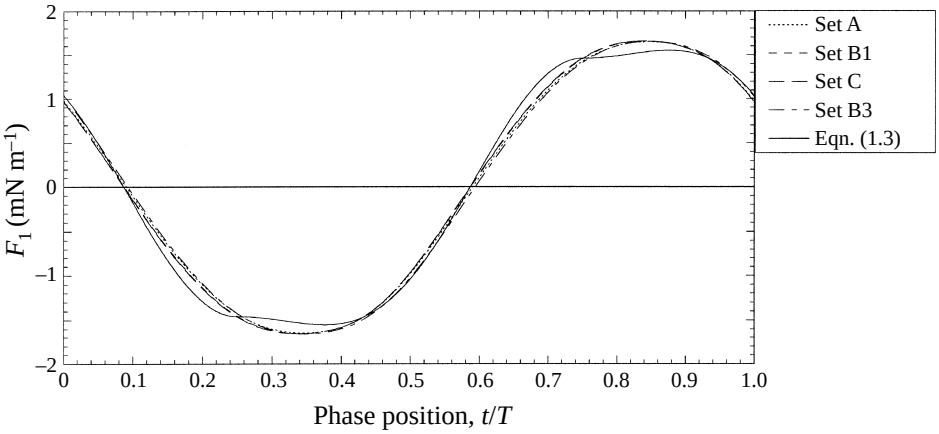

FIGURE 10. In-line force computed on different grid levels at $Re = 100$ and $KC = 5$.

The numerical results allowed the resultant in-line force to be computed with respect to the pressure and shear stress contributions to the total force. This result is provided in figure 9, and shows the dominance of the pressure contribution to the total force. In figure 10 the total force variation with time is presented according to the parameters of the numerical predictions of table 1. The computed results are compared with the $F_1(t)$-time variation predictions according to equation (1.3). This

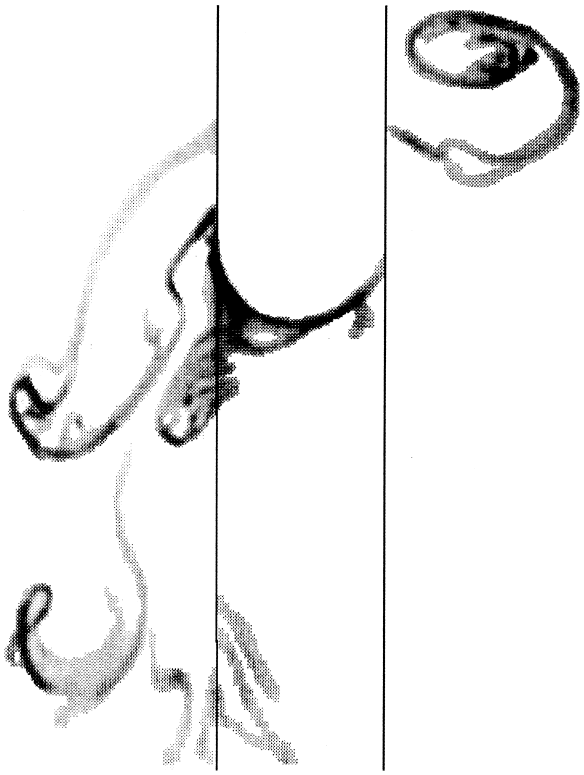

FIGURE 11. Visualized vortex pattern at $Re = 200$ and $KC = 10$.

figure reveals that even the predictions on the coarsest grid and with the largest time step agree better with the most accurately computed time variation of the in-line force than the $F_1(t)$ variation obtained from equation (1.3) and the force coefficients of the best set.

4.2. *Results for* $Re = 200$ *and* $KC = 10$

The present investigations were extended to the parameter combination $Re = 200$ and $KC = 10$, which refers to regime F in figure 4. Carrying out flow visualization experiments revealed a different behaviour of the vortex motion induced by the cylinder oscillation. When starting the cylinder from rest, symmetric vortex shedding occurred first and in roughly the same way as described for the $Re = 100$ and $KC = 5$ case. However, after a few cycles of oscillations, the symmetric flow pattern ceased to exist. The symmetric vortex formation became unstable, resulting in the occurrence of a stronger vortex on one side of the cylinder and a weaker one on the other. This is clearly reflected in figure 11, which also indicates that the difference in the magnitude of the two vortices resulted in a motion of the vortices away from the cylinder at an angle of approximately 27° with respect to the axis along which the cylinder oscillated. Both vortices which were formed did not cross this axis, but moved away from it.

In order to verify that the above-described asymmetric vortex motion could also be obtained through numerical predictions, flow computations were performed for $Re = 200$ and $KC = 10$. The results of these computations are presented in figure 12, showing the same vortex motion as obtained in the experiments.

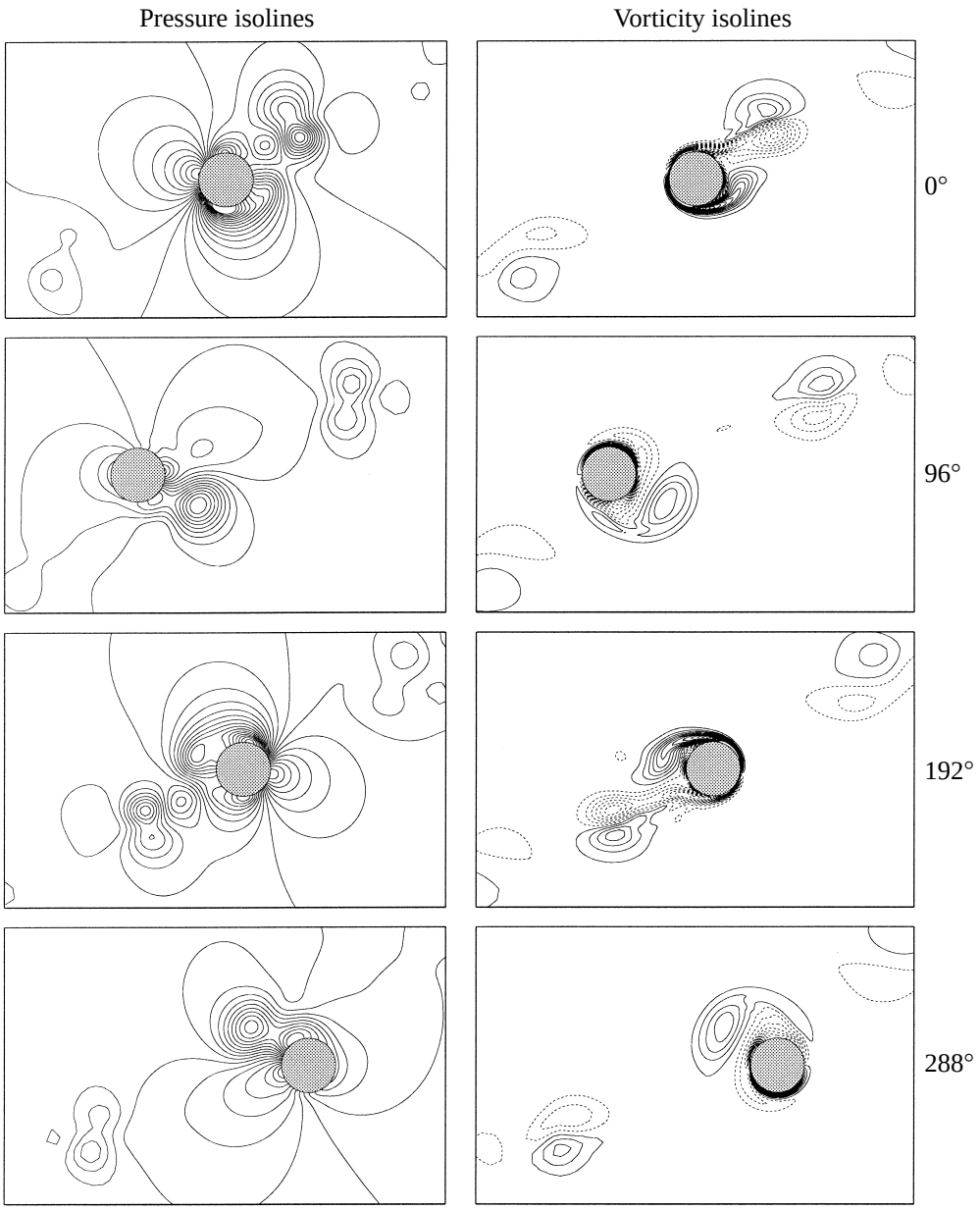

FIGURE 12. Pressure and vorticity isolines (negative values dashed) at $Re = 200$ and $KC = 10$.

Figure 12 clearly shows that two vortex pairs formed within each oscillation cycle and that this formation repeated periodically. In contrast to the vortex formation for $Re = 100$ and $KC = 5$, each pair of vortices consisted of two structures of different age and different initial strength. Each vortex pair existed over several cycles, mainly because it was not divided by the oscillating cylinder motion as in the case $Re = 100$ and $KC = 5$. Finally, a strong inclined vortex street extending in two opposite directions was created by the numerical predictions very similar to those observed in the experiments.

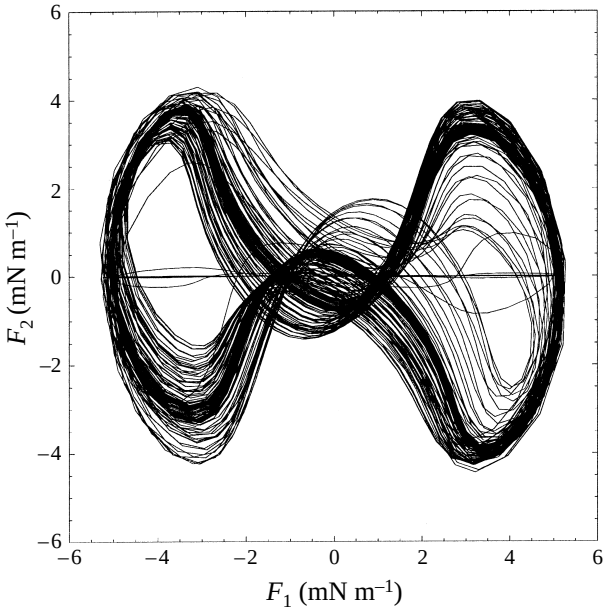

FIGURE 13. In-line and lift force for 100 cycles at $Re = 200$ and $KC = 10$.

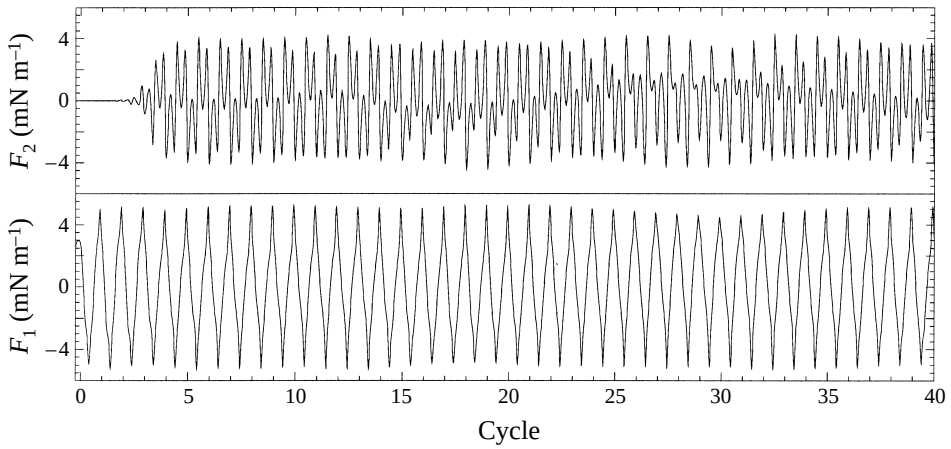

FIGURE 14. In-line and lift force history at $Re = 200$ and $KC = 10$ (set D2).

As the above-described flow field occurs for a cylinder motion along an axis of symmetry, there cannot be a preferred direction of the vortices when they move away inclined to the axis of the cylinder motion. Therefore, the induced flow field possesses two solutions, providing vortex streets inclined positively and negatively with respect to the axis of the cylinder motion. This was also reported by Tatsuno & Bearman (1990) (see their figure 31), where an example of the alternative angle for the vortex street inclination was presented.

In order to investigate further the $Re = 200$ and $KC = 10$ flow case, the authors performed stability investigations of this flow. These revealed that the cyclic flow pattern formation shown in figures 11 and 12 was only weakly stable and therefore showed measurable and predictable deviations from periodicity. This is reflected by

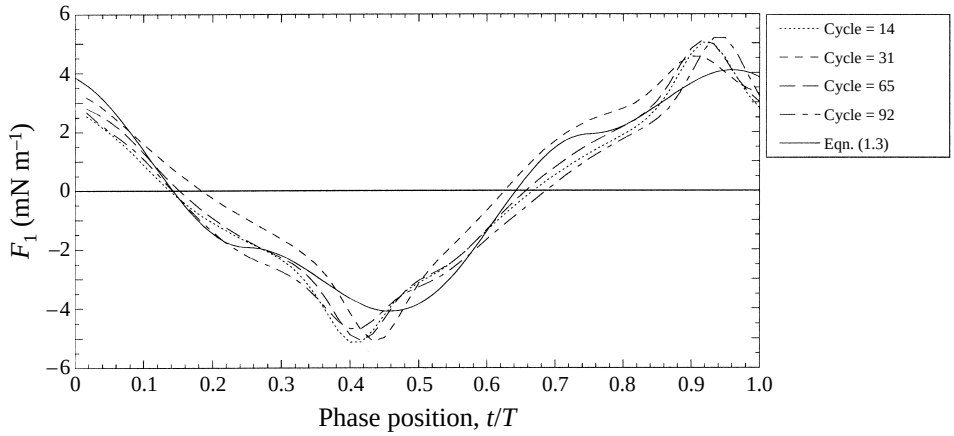

FIGURE 15. Variation of the in-line force between different cycles at $Re = 200$ and $KC = 10$.

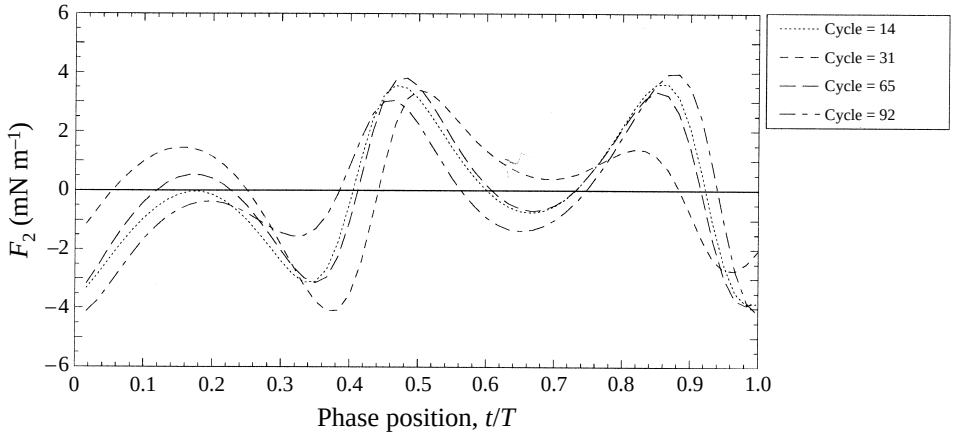

FIGURE 16. Variation of the lift force between different cycles at $Re = 200$ and $KC = 10$.

KC	0.5	1.0	1.5	2.0	3.0	4.0	5.0	6.0	7.0	8.0	9.0	15.0
regime	A*	A*	A*	A*	A*	A	C	E	E/F	F	G	G
c_d	10.4	5.39	3.72	2.98	2.28	1.97	1.82	1.73	1.78–1.79	1.72–1.73	1.80	1.78–1.81
c_i	1.37	1.36	1.35	1.34	1.31	1.30	1.30	1.17	1.07–1.15	1.14–1.15	0.946	0.385–0.511

TABLE 2. Computed drag and added mass-coefficients for $\beta = 35$.

the results of the flow predictions shown in figure 13, presenting the lift force F_2 in relation to the corresponding in-line force F_1 of the oscillating cylinder. Results of 100 oscillation cycles are plotted and these reveal strong cycle-to-cycle variations of the total force vector. Details of the computationally predicted non-periodic results are also shown in figures 14, 15 and 16, showing the strong cycle-to-cycle variations of the forces acting on the oscillating cylinder. Obviously the approach of Morison *et al.* (1950) neglected these findings as the flow is assumed to be fully periodic. Hence, a range of force coefficients is given in table 1. These flow fluctuations were

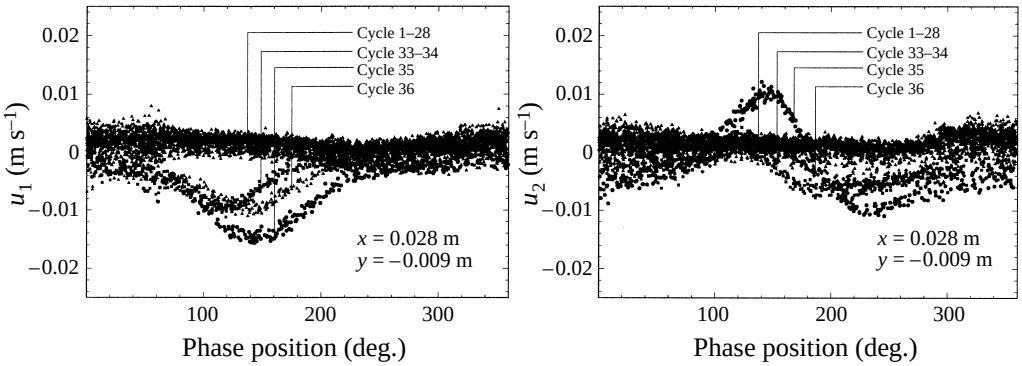

FIGURE 17. Measured cycle-to-cycle data variation at $Re = 200$ and $KC = 10$.

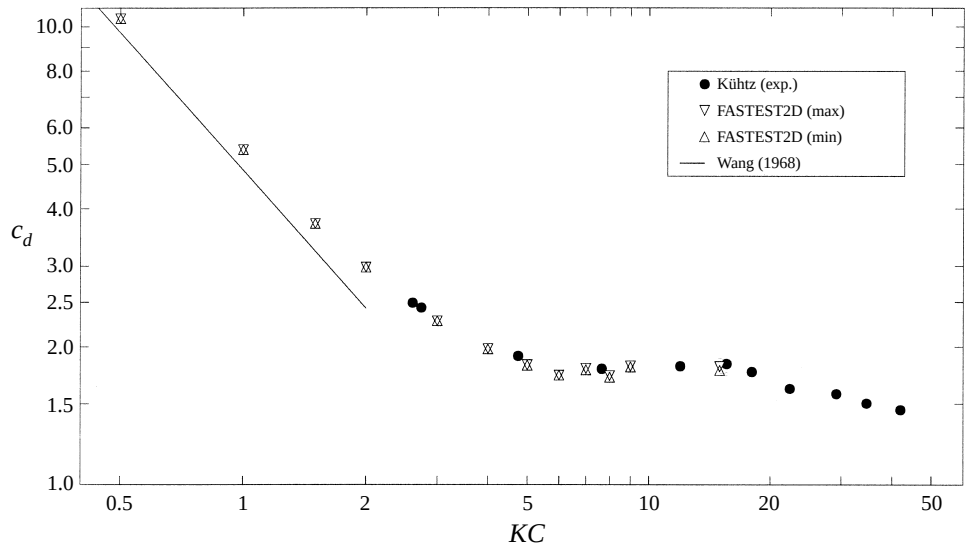

FIGURE 18. Drag coefficients for $\beta = 35$.

also observed in the experiments. Time traces of local velocity measurements are presented in figure 17, revealing remarkable differences between velocities at the same point and for the same phase position, but from different cycles. Beyond this, extreme deviations of single cycles from the mean values were measured, e.g. for cycles 33–36.

4.3. *Results for* $\beta = 35$

Further computations for the ratio $\beta = 35$ were carried out mainly to compare force coefficients with the experimental results of Kühtz (1996). These flow predictions were performed on the fourth grid level with 192 control volumes on the cylinder surface and 24 576 control volumes in the total flow field; 180 time steps were chosen for each cycle of oscillation. The drag and added-mass coefficients derived from these computations are presented in table 2. They were evaluated by Fourier analysis of each cycle neglecting the first 5 to 10. In order to respect noticeable cycle-to-cycle fluctuations, a range of coefficients was calculated. Nevertheless, regarding the in-line force history again deviations between the original and the reproduced functions occurred as already demonstrated in figure 10. The c_m-values were calculated

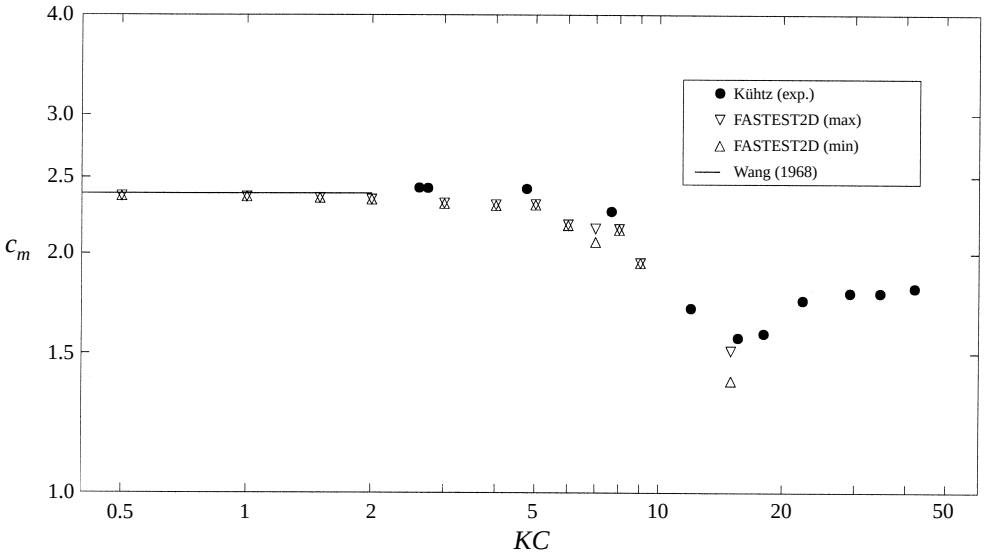

FIGURE 19. Inertia coefficients for $\beta = 35$.

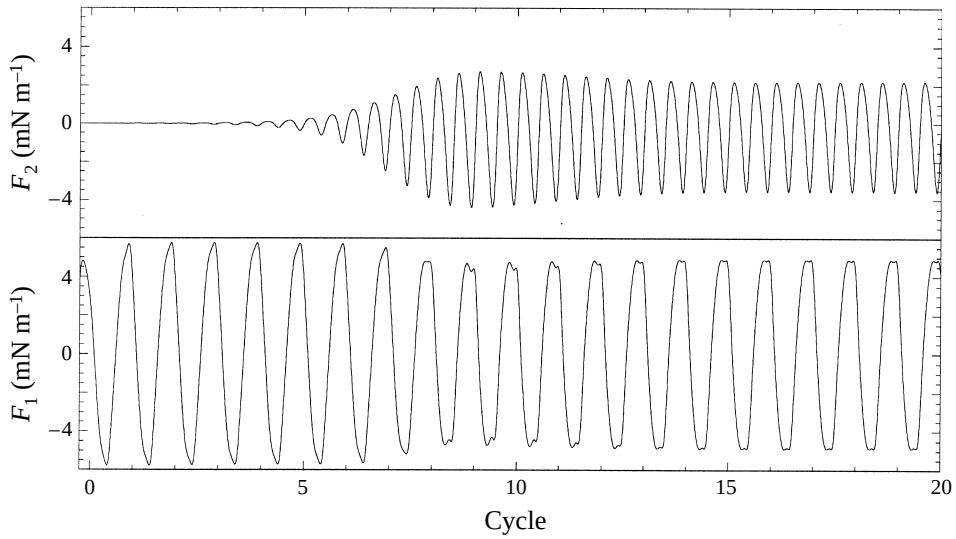

FIGURE 20. In-line and lift force history at $Re = 210$ and $KC = 6$.

according to equation (1.2). The drag and inertia coefficients were then compared with the results of Kühtz (1996) and the well-known theoretical analysis of Wang (1968) (figures 18 and 19). The drag coefficients derived from the numerical predictions were found to be in good agreement and the inertia coefficients to be systematically lower than those from the experiments. Both revealed similar behaviour in comparison with the experiments when increasing KC beyond the two-dimensional regimes. Hence, in some regimes the three-dimensional flow structures seem to have little influence on the in-line force and on the vortex dynamics observed in the plane perpendicular to the cylinder axis. On the other hand considering the results for small values of

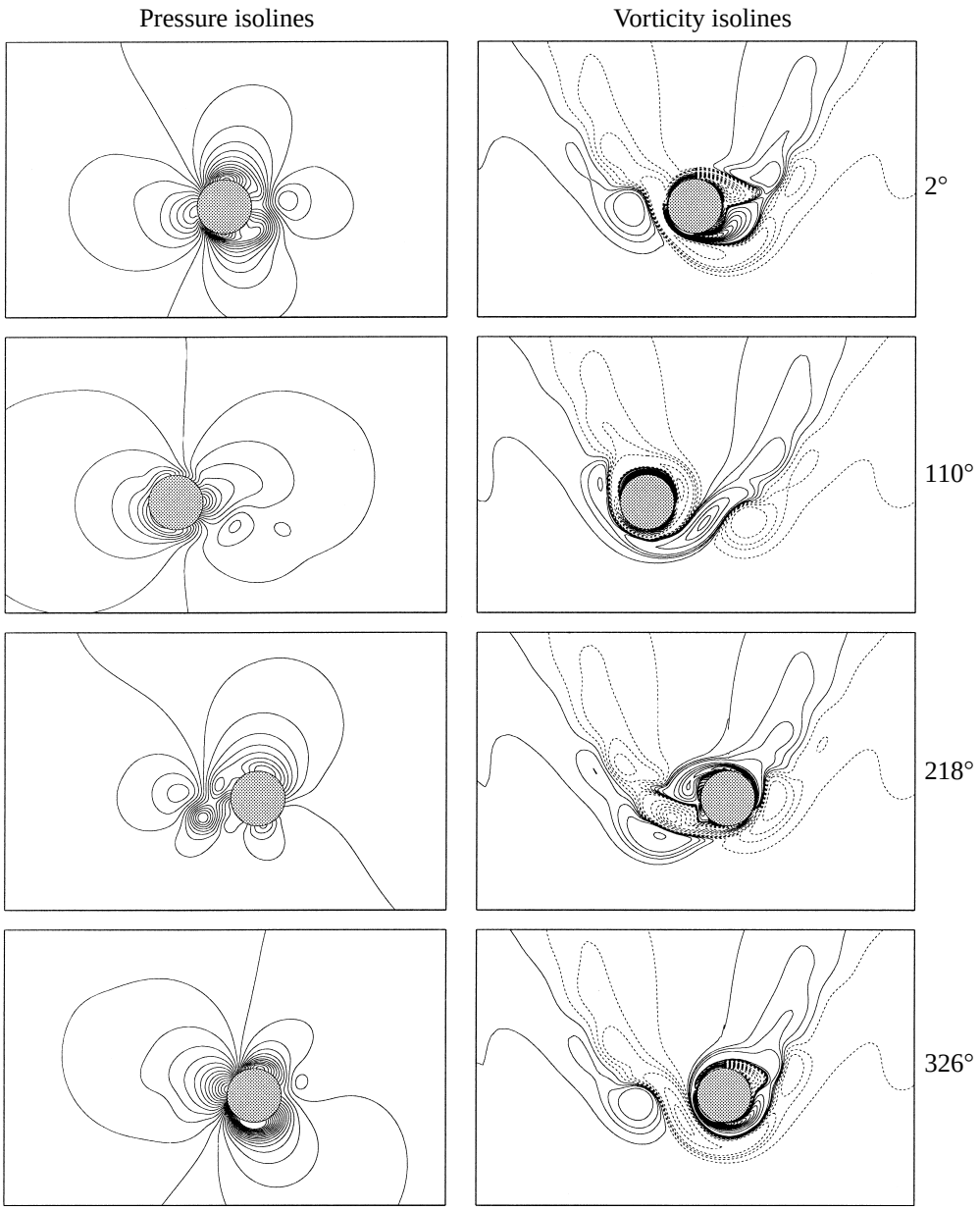

FIGURE 21. Pressure and vorticity isolines (negative values dashed) at $Re = 210$ and $KC = 6$.

KC both coefficients tend asymptotically towards the theory of Wang (1968) giving $c_d = 4.848/KC$ and $c_m = 2.382$ for this case, see Bearman *et al.* (1985).

In order to prove the existence of another fundamental vortex pattern typical of the flow at low Re and KC the parameter combination $Re = 210$ and $KC = 6$ was considered more detailed. According to the classification of Tatsuno & Bearman (1990) the resulting flow belongs to regime E, see figure 4, representing temporarily stable V-type vortex streets.

The computed lift force history, see figure 20, showed that the vortex shedding

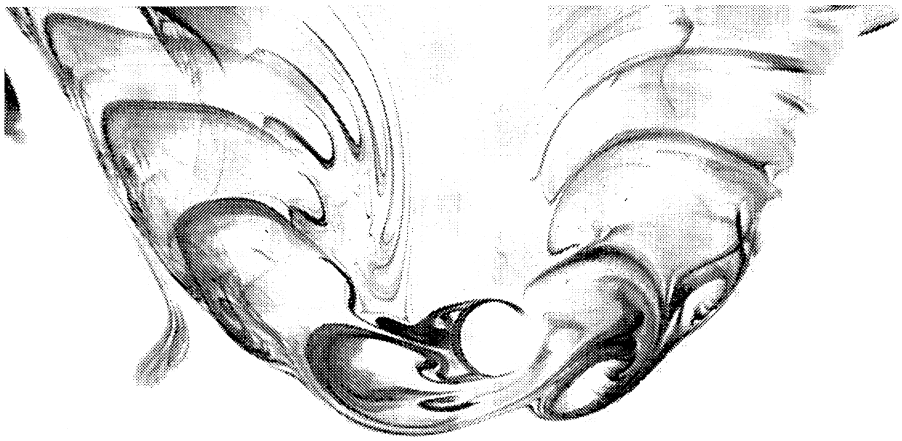

FIGURE 22. Flow pattern in regime E for $KC = 6.28$ and $Re = 161$. Reprint from Tatsuno & Bearman (1990) (figure 23*a*) in reverse colours.

was first symmetric to the plane of oscillation and then became unstable involving a strong increase of the lift force and a slight decrease of the in-line force. After about 15 cycles no more cycle-to-cycle variation occurred. The resulting periodic vortex shedding and motion is presented in figure 21. At different phase positions the pressure distribution and the vorticity isolines in the vicinity of the cylinder are given, demonstrating complex vortex–vortex and cylinder–vortex interactions. While the asymmetry of the vortex shedding near to the cylinder wall is similar to that observed for $Re = 200$ and $KC = 10$, an outer system of vortices could be identified, which was generated the cycle before. As these outer vortices remained near the plane of oscillation they strongly interacted with the boundary layers of the returning cylinder. Therefore their vorticity magnitude decreased rapidly. Finally, pairs of outer vortices were generated in each half of the cylinder period, which were convected to the same side of the plane of oscillation. A global V-type convection pattern resulted, which was much less pronounced than in regime F.

Despite the three-dimensional structures found in experiments, the numerically predicted flow agrees well with the flow visualization shown in figure 22. In the work of Tatsuno & Bearman (1990) it is noted that the direction of convection intermittently changed, and they presumed that this switching of the flow is triggered by small disturbances. But for the computations no artificial disturbances were induced, which stabilized the direction of vortex convection to one side.

5. Conclusions

The present paper summarizes results of experimental and numerical flow investigations with the flow being induced by harmonic oscillations of a cylinder in a fluid at rest. Three cases were considered in detail, characterized by the Reynolds number and Keulegan–Carpenter number combinations $Re = 100$ and $KC = 5$, $Re = 200$ and $KC = 10$ and also $Re = 210$ and $KC = 6$. These cases corresponded to flows belonging to different flow regimes according to the results of Williamson (1985) or the diagrammatic presentation by Tatsuno & Bearman (1990).

For the first set of Re and KC, periodic vortex formations resulted, consisting of vortices with symmetric locations with respect to the line of motion of the oscillating cylinder. Good agreement was obtained between experimental results and

corresponding numerical flow predictions. This good agreement confirms that both the experimental and the numerical results are sufficiently accurate to yield physically reliable information on the time-dependent flow induced by oscillatory cylinder motion. Hence, computer codes to predict the oscillatory fluid motion and to deduce the lift and in-line force information are readily employable within the investigated parameter range.

The flow pattern obtained for $Re = 200$ and $KC = 10$ differed drastically from that for $Re = 100$ and $KC = 5$ as well as for $Re = 210$ and $KC = 6$. The vortex formation turned out to be asymmetric, yielding a vortex street that moved along a line which was inclined with respect to the direction of motion of the oscillating cylinder. This flow turned out to be only weakly stable, resulting in cycle-to-cycle variations of the local flow properties. The cycle-to-cycle variations were also found when considering the forces acting on the cylinder. The numerical findings regarding the weak stability of the flow pattern as well as the vortex dynamics for $Re = 200$ and $KC = 10$ were confirmed by the experiments carried out for this parameter set, although three-dimensional flow occurs in this regime.

A third fundamentally different vortex pattern was found, on investigating the flow field numerically for $Re = 210$ and $KC = 6$. Vortex pairs convected periodically to the same side of the plane of oscillation creating a V-type pattern. Good agreement with experimental flow visualization and force coefficients was observed as well as for other results at $\beta = 35$, which tended asymptotically towards the theory of Wang (1968). Nevertheless, good agreement was obtained not only for the regimes A^* and A, where two-dimensional flow was found, but also in regimes where three-dimensional structures arise along the cylinder axis.

These results as well as those of other authors, e.g. Lin *et al.* (1996), clearly confirm that both flow field and force coefficients can be reliably obtained by numerical solution of the governing fluid mechanics equations within the present range of parameters.

For future investigations the coupled numerical simulation of the response of an elastically mounted structure to fluid flow excitation, see e.g. Newman & Karniadakis (1995), will be of major interest. The right-hand side of the equation of motion of a structure would be determined directly by the flow field predictions, taking into account all effects of vortex shedding and vortex dynamics in time.

This work was sponsored by a grant from the Bavarian Consortium for High Performance Computing, FORTWIHR, and by the European Union under a SCIENCE contract, which the authors gratefully acknowledge. The authors are also grateful to Prof. M. Tatsuno for allowing them to reprint his figure, and to Dr S. Kühtz for helpful communications.

REFERENCES

Anagnostopoulos, P., Iliadis, G. & Ganoulis, J. 1995 Flow and response parameters of a circular cylinder vibrating in-line. In *Flow-Induced Vibration* (ed. P. W. Bearman), Rotterdam, pp. 167–179. Balkema.

Bearman, P. W., Downie, M. J., Graham, M. R. & Obasaju, E. D. 1985 Forces on cylinders in viscous oscillatory flow at low Keulegan-Carpenter numbers. *J. Fluid Mech.* **154**, 337–356.

Bearman, P. W., Lin, X. W. & Mackwood, P. R. 1992 Measurement and predicition of response of circular cylinders in oscillating flow. In *Behaviour of Offshore Structures*, vol. 6, pp. 297–307.

Blevins, R. D. 1977 *Flow-Induced Vibration.* Van Nostrand Reinhold.

Durst, F., Perić, M., Schäfer, M. & Schreck, E. 1993 Parallelization of efficient numerical methods for flows in complex geometries. *Notes Numer. Fluid Mech.* **38**, 79–92.

FASTEST - Parallel Multigrid Solver for Flows in Complex Geometries manual 1994. Invent Computing GmbH Erlangen.

Justesen, P. 1991 A numerical study of oscillating flow around a circular cylinder. *J. Fluid Mech.* **222**, 157–196.

Keulegan, G. H. & Carpenter, L. H. 1958 Forces on cylinders and plates in an oscillating fluid. *J. Res. Natl Bur. Stand.* **60**, 423–440.

Knörnschild, U. 1994 Experimentelle Untersuchungen der Strömungsverhältnisse um einen oszillierenden Kreiszylinder. Master's thesis, University of Erlangen-Nürnberg, LSTM, Erlangen.

Kühtz, S. 1996 Experimental investigation of oscillatory flow around circular cylinders at low beta numbers. PhD thesis, University of London.

Kühtz, S., Bearman, P. W. & Graham, J. M. R. 1997 Problems encountered in measuring forces on immersed bodies. *Expl Techniques* **21**, 20–23.

Lienhart, H. & Böhnert, T. 1992 Grenzschichtmessungen an einem Laminarflügelprofil mit einem Laser-Doppler-Anemometer, 8. *DGLR-Fach-Symp. STAB, Köln. DGLR-Bericht* 94–04 .

Lin, X. W., Bearman, P. W. & Graham, J. M. R. 1996 A numerical study of oscillatory flow about a circular cylinder for low values of beta parameters. *J. Fluids Struct.* **10**, 501–526.

Morison, J. R., O'Brien, M. P., Johnson, J. W. & Schaaf, S. A. 1950 The force exerted by surface waves on piles. *Petrol. Trans. AIME* **189**, 149–154.

Newman, D. J. & Karniadakis, G. E. 1995 Direct numerical simulation of flow over a flexible cable. In *Flow-Induced Vibration*. Rotterdam: Balkema.

Naudascher, E. & Rockwell, D. 1994 *Flow-Induced Vibrations, An Engineering Guide*. Rotterdam: Balkema.

Obasaju, E. D., Bearman, P. W. & Graham, J. M. R. 1988 A study of forces, circulation and vortex patterns around a circular cylinder in oscillating flow. *J. Fluid Mech.* **196**, 467–494.

Patankar, S. V. 1980 *Numerical Heat Transfer and Fluid Flow*. Hemisphere.

Sarpkaya, T. 1976 Vortex shedding and resistance in harmonic flow about smooth and rough circular cylinders at high Reynolds numbers. *Tech. Rep.* NPS-59SL76021, Naval Postgraduate School, Monterey.

Sarpkaya, T. 1986 Force on a circular cylinder in viscous oscillatory flow at low Keulegan–Carpenter numbers. *J. Fluid Mech.* **165** , 61–71.

Sarpkaya, T.1992 Recent progress in basic numerical and physical experiments on oscillating flow about cylinders. In *Second Osaka Intl Colloq. on Viscous Fluid Dynamics*, vol. 1, pp. 35-74.

Sarpkaya, T., Putzig, C., Gordon, D., Wang, X. & Dalton, C. 1992 Vortex trajectories around a circular cylinder in oscillatory plus mean flow. *J. Offshore Mech. Arctic Engng* **114**, 291-298.

Stansby, P. K. & Smith, P. A. 1991 Viscous forces on a circular cylinder in orbital flow at low Keulegan-Carpenter numbers. *J. Fluid Mech.* **229**, 159–171.

Tatsuno, M. & Bearman, P. W. 1990 A visual study of the flow around an oscillating circular cylinder at low Keulegan–Carpenter numbers and low Stokes numbers. *J. Fluid Mech.* **211**, 157–182.

Troesch, A. W. & Kim, S. K. 1991 Hydrodynamic forces acting on cylinders oscillating at small amplitudes. *J. Fluids Struct.* **5**, 113–126.

Wang, C.-Y. 1968 On high-frequency oscillatory viscous flows. *J. Fluid Mech.* **32**, 55–68.

Williamson, C. H. K. 1985 Sinusoidal flow relative to circular cylinders. *J. Fluid Mech.* **155**, 141–174.